Infrasound measurements from a tornado in Oklahoma

Brian R. Elbing, Christopher E. Petrin, and Matthew S. Van Den Broeke

---

ARTICLES YOU MAY BE INTERESTED IN

Monitoring infrasound from a Tornado in Oklahoma
The Journal of the Acoustical Society of America **143**, 1808 (2018); https://doi.org/10.1121/1.5035924

Measurement and characterization of infrasound from a tornado producing storm
The Journal of the Acoustical Society of America **146**, 1528 (2019); https://doi.org/10.1121/1.5124486

Role of clay particle electrostatics and dielectric permittivity of silt particles in sound attenuation in mud
Proceedings of Meetings on Acoustics **30**, 005005 (2017); https://doi.org/10.1121/2.0001016

Impulse noise measurements of M16 rifles at Marine Base Quantico
Proceedings of Meetings on Acoustics **33**, 040003 (2018); https://doi.org/10.1121/2.0001010

Computation of dispersion curves of guided waves in functionally graded materials
Proceedings of Meetings on Acoustics **33**, 045002 (2018); https://doi.org/10.1121/2.0001014

Physics of musical drum head damping using externally applied products
Proceedings of Meetings on Acoustics **35**, 035004 (2018); https://doi.org/10.1121/2.0001011

175th Meeting of the Acoustical Society of America

Minneapolis, Minnesota

7-11 May 2018

Physical Acoustics: Paper 2pPA8

Infrasound measurements from a tornado in Oklahoma

Brian R. Elbing and Christopher E. Petrin
Department of Mechanical & Aerospace Engineering, Oklahoma State University Stillwater, Stillwater, OK, 74078; elbing@okstate.edu; cepetri@okstate.edu

Matthew S. Van Den Broeke
Department of Earth and Atmospheric Sciences, University of Nebraska-Lincoln, Lincoln, NE, 68588; mvandenbroeke2@unl.edu

Tornado-producing storms have been observed to emit infrasound (sound at frequencies below human hearing) up to 2 hours before tornadogenesis. Weak atmospheric attenuation at these frequencies allows for long-range detection. Hence, passive infrasonic monitoring could be a method for long-range studying of tornadogenesis as well as tornado characterization. Identifying the fluid mechanism(s) responsible for infrasound production is key to enabling such capabilities, but currently there are insufficient detailed observations to test potential mechanisms. Thus this paper documents infrasound recordings from ~19 km away from a small unrated (EFU) tornado that formed near Perkins, Oklahoma (35.97, -97.04) at 2013 UTC on 11 May 2017. Analysis of the recording shows that from 4 minutes before to 40 minutes after tornadogenesis spectral peaks formed in the 5-50 Hz band. The bearing angle of this signal tracked with the storm core that produced the tornado. It was also shown that the fundamental frequency associated with the tornado was 8.3 Hz with overtones at 18, 29, 36, and 44 Hz. These overtones are linearly related with the mode number, but are not pure harmonics with a factor of 1.1 between frequencies. In addition, the spectral content was compared with available radar data.

1. INTRODUCTION

The 5-year average for tornado warning lead times is 8.6 ± 0.6 min with a probability of detection (POD) of 59% and a false alarm rate (FAR) of 70% (NOAA, 2018). These numbers indicate a decrease in tornado warning effectiveness relative to ~10 years ago. In part, this has motivated research on identifying new approaches that could improve tornado warnings. Several researchers have observed that tornadoes emit infrasound (Bowman & Bedard, 1971; Bedard, 2005; Frazier et al., 2014; Dunn et al.; 2016), sound below human hearing, in the 0.5-10 Hz band with some signals detected well in advance of tornadogenesis. Infrasound is a potentially valuable approach because it can be passively detected from long range due to weak atmospheric absorption at these frequencies and an "acoustic ceiling" (Bedard & Georges, 2000). The most recent detailed analysis was Frazier et al. (2014), which examined high-fidelity acoustic recordings covering the frequency range from 0.2 to 500 Hz from three tornadoes in Oklahoma. Primary findings from this work are the use of beamforming at infrasound frequencies to track long-duration tornadoes, detection of audible frequency sound, and demonstration of a modified aeroacoustic jet turbulence model to predict the observed signature in the audible frequency range. However, there is still a dearth of detailed observations of tornado infrasound. Therefore, this paper serves as documentation of an infrasound recording during a weak tornado and assesses the likelihood that the received signal was associated with the tornado.

2. DATA ACQUISITION

A. INFRASOUND

A 3-microphone (Model 24, Chaparral Physics) infrasonic array was deployed on the campus of Oklahoma State University (OSU) during the 2017 tornado season. This effort was part of the CLOUD-MAP project (Elbing & Gaeta, 2016; Smith et al., 2017; Jacob et al., 2018), a multi-university collaboration focused on the development and implementation of unmanned aerial systems (UAS) and their integration with atmospheric sensors. The infrasonic array, shown in Figure 1, was centered at (36.1344, −97.0815) with microphone 1 located on a building roof (36.1344, −97.0819) and the other two (microphone 2: 36.1342, −97.0812; microphone 3: 36.1347, −97.0814) located at ground level. This places the distance between microphones 1-2, 1-3, and 2-3 at 67.6 m, 58.6 m, and 58.5 m, respectively. Each microphone had a nominal sensitivity of ~400 mV/Pa and a nearly flat response from 0.1-200 Hz. All the microphones had identical mounting structure that included a low-frequency vibration isolation pad with the microphone sealed within an acrylic dome painted white.

Figure 1. Satellite image of the OSU infrasonic array with microphone locations labelled and denoted by the 'X'.

Windscreens were produced using four 15-m long porous hoses connected to each microphone for spatial averaging to cancel out incoherent noise (e.g., wind). The microphones with and without the windscreens (hoses) were tested in an anechoic chamber (though not anechoic to infrasound frequencies) in a method similar to that of Hart & McDonald (2009). These results showed significant reduction in wind noise below 50 Hz without significant attenuation of a reference signal, but no noise reduction by 100 Hz (Threatt, 2016). The microphones were powered with DC-power supplies (APS-1303, Aktakom). The output from each microphone was recorded via a dynamic signal analyzer (USB-4432, National Instruments). The data acquisition was controlled via a commercial software package (Sound & Vibration Measurement Suite, National Instruments). The sample rate

was fixed at 1 kHz and grouped in 20-minute observation windows. Unfortunately, there was cross-talk between microphones 2 and 3 that was not identified until after the reported observation.

B. RADAR

Data were analyzed from the Weather Surveillance Radar-1988 Doppler (WSR-88D) at Oklahoma City, Oklahoma (KTLX; 35.33306, -97.27778), which is located ~70 km southwest of the verified tornado. At this range, the base-scan radar beam height was ~0.95 km above radar level (ARL). Data were analyzed from 1928 UTC on 11 May 2017 (~45 min prior to tornadogenesis) to 2103 UTC, when the storm became too far from the radar for good data quality. Around this time, other nearby storms began to become dominant and merge with the storm of interest.

C. GROUND-LEVEL ATMOSPHERIC MONITORING

Ground-level atmospheric conditions were monitored with Oklahoma Mesonet stations (Brock et al., 1995; McPherson et al., 2007) and a weather station located ~0.17 km south of the infrasonic array (termed DML). The DML weather station (Vantage Pro, Davis Instruments) was located on a building roof and provided 30-minute averages of temperature, humidity, atmospheric pressure, and wind speed. The Oklahoma Mesonet network consists of 120 automated environmental monitoring stations that measure air temperature 1.5 m above ground, relative humidity 1.5 m above ground, wind speed and direction 10 m above ground, barometric pressure, rainfall, incoming solar radiation, and soil temperature. Data are packaged in 5 min "observations" that are quality checked by the Oklahoma Climatological Survey prior to being released. The current study used three sites; Perkins (PERK), Stillwater (STIL), and Marena (MARE).

3. STORM CHARACTERIZATION

A. OVERVIEW

On 11 May 2017 a line of storms to the west of the infrasonic array included a hail-producing supercell. At 2013 UTC the supercell produced an EFU tornado (the "U" indicates an unknown rating) near Perkins, OK (35.97, -97.04), which was located 18.7 km south-by-east (SbE) of the infrasonic array. The official tornado path length and damage width were 0.16 km (0.10 miles) and 46 m (150 ft) (NOAA, 2017), respectively. There were live news reports of a possible second tornado after the first, but it was never confirmed due to the storm being rain wrapped and no low-level radar coverage. There were a total of 15 confirmed hail events associated with this storm, but only one occurred within 10 minutes of the confirmed tornado. The ground-level monitoring stations (STIL, MARE, PERK, DML) showed similar trends in air temperature, relative humidity, wind speed, and wind direction over the two hours before and after the tornado. The only significant variations were higher speeds at the PERK site when the tornado was present and the temperature drops earlier at the MARE site due to it being farther west. Of particular note, the wind direction at PERK from ~10 minutes before the tornado through the life of this storm was aligned with the direction from the tornado to the infrasound array. The resulting mean speed of sound between the STIL, DML, and PERK sites was 343.8 m/s, which was computed assuming humid air (Cramer, 1993). However, there was only a 0.03% deviation from using the dry air calculation ($c = \sqrt{\gamma R T_K}$), where c is the speed of sound, γ is the ratio of specific heats ($\gamma_{air} \approx 1.4$), R is the specific gas constant ($R_{air} = 287$ J/kg·K), and T_K is the absolute temperature.

B. RADAR ANALYSIS

Several radar metrics were analyzed through the analysis period for the storm of interest (11 May 2017 from 1928-2045 UTC). Base-scan data (radar reflectivity factor and radial velocity) at an altitude of ~0.88 km ARL near the storm core at 1953 UTC are shown in Figure 2. The velocity difference near the surface and associated with the tornadic vortex cannot be robustly analyzed for this event because of its distance from the radar site. Compounding this problem is the small size of the tornado (~50 m max width at the ground), meaning that radar observations at this distance are incapable of measuring maximum wind speeds toward and away from the radar within the tornado. Instead, maximum radial velocity difference (MRVD) was derived for the low-level mesocyclone at base scan, at an altitude of ~1 km ARL. This storm had a well-defined mesocyclone (Figure 2b), so maximum velocity difference was computed as the difference between the associated maximum inbound and outbound velocities. This analysis was done from 1928-2045 UTC, since beyond this time the storm-radar distance increased to too large of a value for velocity difference values to remain comparable.
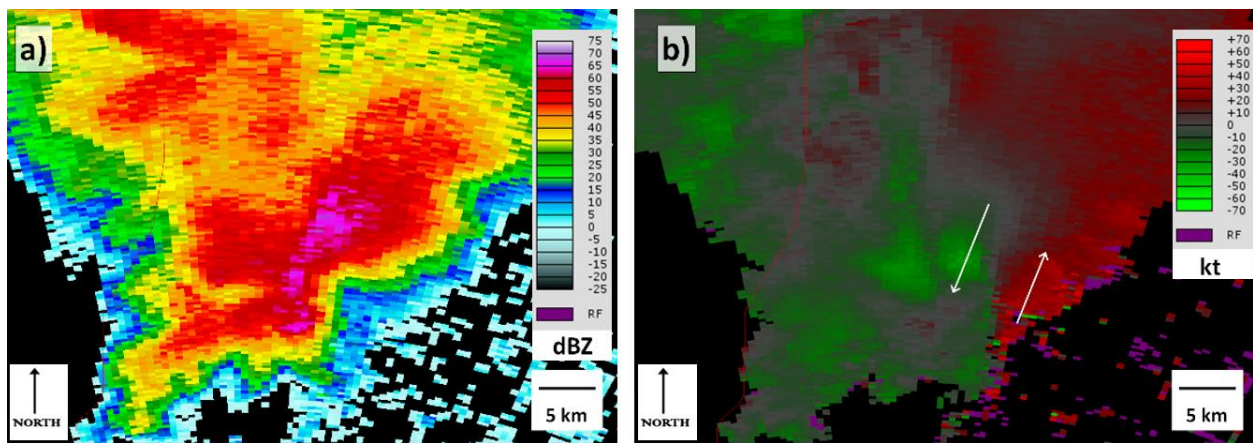
Figure 2. (a) Radar reflectivity factor and (b) radial velocity from KTLX at 1953 UTC on 11 May 2017. Data are base-scan, with an altitude of ~0.88 km ARL near the storm core. Arrows in (b) indicate the inbound and outbound velocities associated with the low-level mesocyclone.

Through the analysis period, the MRVD in the low-level mesocyclone ranged from 13.5 m/s to 42.5 m/s (Figure 3a). The mesocyclone was relatively weak for a few time steps after initiating, but was well-defined and reasonably strong by 1940 UTC (Figure 3a - MRVD). The low-level mesocyclone reached its maximum intensity at 2000 UTC, ~13 min prior to reported tornadogenesis. Shortly after tornadogenesis, intensity of the low-level mesocyclone decreased sharply and did not recover during the analysis period. Radar beam-centerline altitude did not change substantially with the low-level mesocyclone intensity, indicating that the observed MRVD changes were genuine changes to storm organization and not an effect of radar beam propagation.
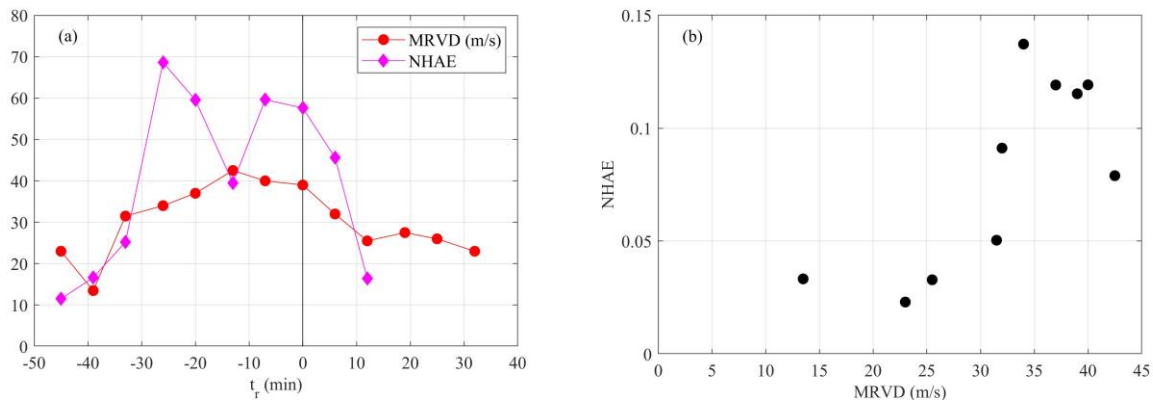

Figure 3. (a) Time series of maximum radial velocity difference (MRVD) and of normalized hail areal extent (NHAE) from 1928-2025 UTC. NHAE has been multiplied by 500 to fit on the same scale. (b) Scatterplot of MRVD versus NHAE. One data point is present for each base scan from 1928-2025 UTC.

A compilation of infrasound observations from severe hail-producing storms over a 10-year period (Bowman & Bedard, 1971) showed a nearly linear relationship between hail diameter and infrasound period (10 to 50 sec). Motivated in part by these observations, Bedard (2005) provided an in-depth analysis of two significant hail producing storms with no evidence of vorticity (i.e. no observed tornado, funnels, or mesocyclone). There was no acoustic energy detected from either storm, which indicates that infrasound is not simply a common feature of severe weather. A recent simulation of infrasound from a tornado-like vortex shows that the dominant infrasound in the 0.1-10 Hz frequency range appears to radiate from the vicinity of the melting level, where diabatic processes involving hail are active (Schecter et al., 2008). Given the potential relationship between hail production and infrasound, the base-scan normalized hail areal extent (NHAE) > 35 dBZ in radar reflectivity factor (Z_{HH}) (Van Den Broeke, 2017) was also analyzed. NHAE uses a combination of Z_{HH} and differential reflectivity (Z_{DR}; e.g., Doviak & Zrnić, 2006) to identify areas where hail is present. NHAE is normalized by the storm area, which makes it a percentage of the base-scan storm area > 35 dBZ dominated by hail and allows for comparison between storms. The time history of the normalized hail areal extent (NHAE) (multiplied by 500 so the magnitude is comparable to MRVD) is also shown in Figure 3a. An initial burst of hail

around 1947 UTC ($t_r \approx -26$ min) is followed by a second burst of hailfall from 2006-2013 UTC. Prior work has noted that hailfall is often maximized in the minutes leading up to tornadogenesis (Browning, 1965; Van Den Broeke et al., 2008). Area of the storm dominated by hail decreased markedly after tornado demise (Figure 3a). A scatterplot of low-level mesocyclone MRVD versus NHAE (Figure 3b) shows that the two variables are well-correlated (Pearson's correlation = 0.75); a large amount of storm area contains hail when the mesocyclone is relatively intense.

4. INFRASOUND OBSERVATIONS

A. INFRASOUND CHARACTERIZATION

I. TIME SERIES

Studying infrasound from any geophysical source has two primary challenges, definitively identifying (and isolating) the infrasonic signal and quantifying sound propagation effects. The infrasound community has made great advances in the study of acoustic propagation of infrasound (Le Pichon et al., 2010; Waxler & Assink, 2017). For the current work, no corrections for propagation effects have been applied since the primary objective is to assess the likelihood that the received infrasound signal was associated with the tornado that formed close to the infrasound array. The criteria commonly used for source identification/detection are concomitancy, characteristic signature, coherence, and directionality (Shams et al., 2013; Elbing & Gaeta, 2016). Given limited radar data and noise contaminated infrasound data, detection of the tornado was not possible, but it is possible to assess if the measured signals are consistent with a nearby tornado. The time trace of microphones 1 and 3 are provided in Figure 4 with the time (t_r) relative to the tornado report (11 May 2017, 2013 UTC). Microphones 3 data is included because it contains independent data that has been contaminated with the "noise" from microphone 2. This shows that an infrasound signal that was above the background levels was present on both microphones, appears to have two bursts (or events) with the peak of the first event coinciding with the verified tornadogenesis ($t_r = 0$), and elevated background levels after the second burst/event.
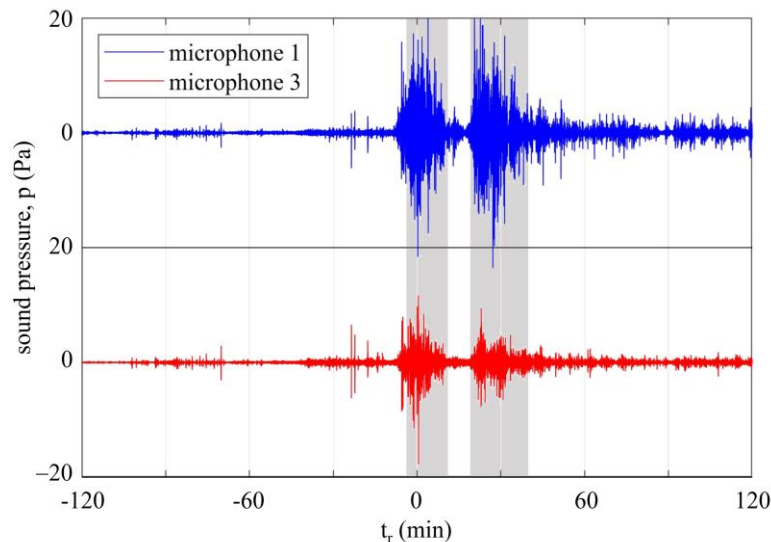

Figure 4. The measured sound pressure versus time in minutes relative to the tornado touchdown (11 May 2017, 2013 UTC) for microphones 1 and 3 with the amplitude of microphone 3 shifted for clarity. The shaded regions correspond to event periods that will be discussed subsequently.

II. SPECTRAL ANALYSIS

To analyze the sound pressure spectra, a period of interest needs to be identified as well as the window size used to segment the period of interest. A tornado is a singular nonstationary event, which makes many of the traditional processing and analysis techniques invalid. However, for the purpose of analysis such signals can often be viewed as piecewise stationary if an appropriate averaging window can be identified. In general, increasing the averaging window T reduces random errors but increases bias errors. Here the trial-and-error analysis method of Bendat & Piersol (2000) for nonstationary single records was followed. The time trace of the

squared effective pressure, $P_e^2 = \frac{1}{T}\int_0^T p^2 dt$, with progressively larger T from 0.01 s to 1000 s was used to identify the appropriate window size. This showed that with $T = 100$ s the random errors were minimized without significant increases in bias errors. Identifying the periods of interest for analysis is more challenging. The cross-correlation between the sound pressures from microphones 1 and 3, $C_{1,3}(t) = \frac{1}{T}\int_0^T P_1(\tau)P_3(\tau + t)d\tau$, was computed to assess the similarity between the signals, where τ is the lag (or shifted) time between signals. The time trace from 30 minutes before to 60 minutes after the tornado report is provided in Figure 5 with the sample intervals set at 100 sec with 50% overlap. Inspection of these results shows that the period of interest starts at approximately $t_r \approx -7$ min and extends to $t_r \approx +52$ min with a quiet period between the two infrasound bursts/events (11 min $< t_r < 19$ min).
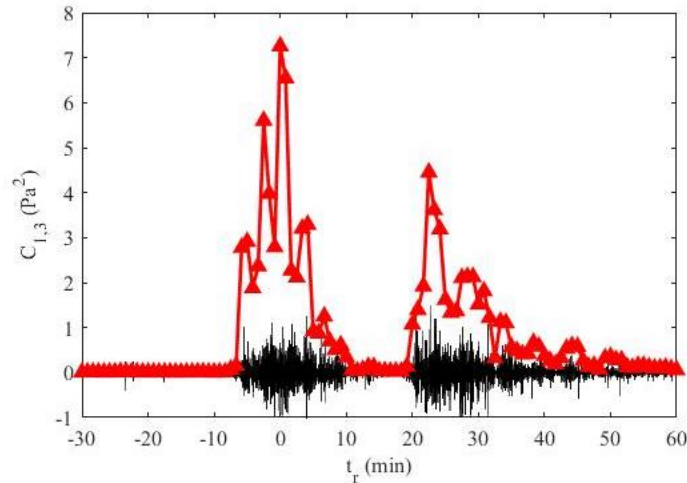

Figure 5. Time trace of the cross-correlation between microphones 1 and 3. The normalized sound pressure from microphone 1 (thin black line) has been included for reference.
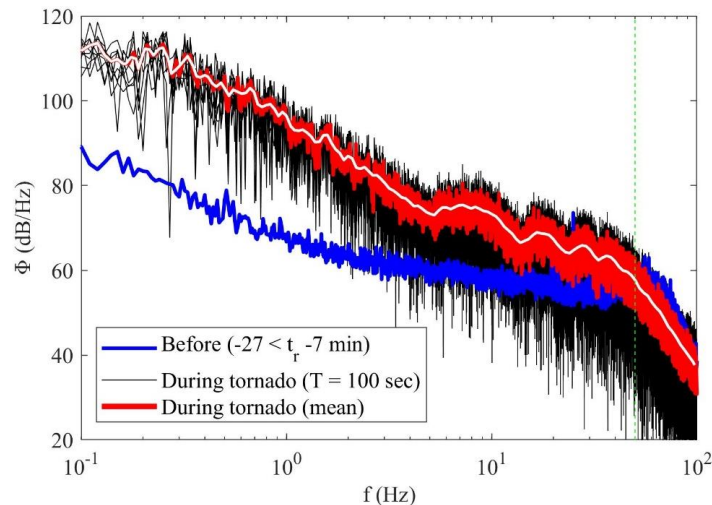

Figure 6. Sound pressure spectra during the nominal time of arrival of signals emitted from the verified tornado ($-46 < t_r < 154$ s) compared with the sound pressure spectra before the rise in infrasound (blue line). Thin black lines correspond to spectra from individual 100 sec intervals, and the thin white line is the mean with a $1/50^{th}$ decade filter applied.

The sound pressure spectra, $\Phi(f)$, presented herein are the single-sided form such that

$$P_{rms}^2 = \int_0^\infty \Phi(f)df, \tag{1}$$

where P_{rms}^2 is the pressure variance and f is the temporal frequency. First it is informative to examine the power spectra corresponding to the period of time when the tornado was present. Given the orientation of the tornado relative to the infrasound array, the acoustic wave would require at least 54 seconds to reach the array. Since the

averaging window size (100 sec) is nominally consistent with the level of accuracy of when the tornado was present, the window used to analyze the period when the tornado was present was set at $-46 < t_r < 154$ s. This period was analyzed in 100 sec segments with 75% overlap between segments. The accuracy of each spectrum was checked against (1), and the variation was less than 1% for all computed spectra. The resulting spectra reported in decibels reference to 20 µPa from each segment (as well as the mean with and without a smoothing $1/50^{th}$ decade filter) from microphone 1 is compared against the background levels before the tornado in Figure 6. Here there is gradual decay in the power spectral density from ~0.1 Hz until a broad peak is observed between 5 and 14 Hz. The elevated spectral levels below 5 Hz are likely due to wind noise, which is further assessed subsequently. The broad 5-14 Hz peak was smoothed with a $1/50^{th}$ decade filter and then the maximum energy was used to identify the peak of 75 dB at 8.3 Hz with a quality factor of 1.6. The quality factor $\left(Q = f_{pk}/(f_U - f_L)\right)$ is a measure of the bandwidth of the peak, where f_U and f_L are the frequency 3 dB below the peak on the upper and lower side of the peak, respectively. Following the initial peak at ~8.3 Hz, there are overtones with nominal peaks at 18, 29, 36, and 44 Hz, which have quality factors (Q) of 3.4, 3.8, 4.8, and 4.9, respectively. After the last overtone there is a rapid roll-off associated with the low-pass filter created by the porous hose windscreens. The fundamental frequency (8.3 Hz) peak was ~18 dB above the levels before the rise in infrasound associated with the tornado ($-27 < t_r < -7$ min).

With the spectra during the verified tornado identified, it is informative to examine the time history of the power spectra to determine when this signal (particularly in the 5-50 Hz) range was present. Examination of the evolution of the power spectra throughout the entire window of interest (-7 min < t_r < 52 min) shows that the tones in the 5-50 Hz range first appear at ~4 minutes before touchdown (t_r = -4 min), even though the background infrasound increases earlier. This is illustrated in Figure 7a, which compares the spectrum during the elevated period before the tones form (-7 min ≤ t_r ≤ -4 min) with the mean spectrum during the first event/burst (-4 min ≤ t_r ≤ 11 min) as well as the spectrum before (-30 min ≤ t_r ≤ -7 min) and after (52 min ≤ t_r ≤ 60 min) the period of interest. This shows that for the short window before t_r = -4 min, the infrasound was elevated above the background but no tones formed. Similarly, for the period after t_r = +40 min the tones are no longer present even though the infrasound remains slightly elevated above the background levels. Thus events 1 and 2 are defined based on the periods when the infrasound was elevated and the tones were present, (-4 min < t_r < 11 min) and (19 min < t_r < 40 min), respectively. Figure 7b compares the spectra during event 1, event 2, and between events with the spectrum before and after the period of interest. This shows that events 1 and 2 had nearly identical spectra as that observed during the tornado, and that even the quieter period between the events had similar (though reduced) spectra. This suggests that the same mechanism was active throughout the period of interest with the source either weakening for a period or the propagation path changing (e.g. wind speed/direction, source elevation, storm structure, etc.).
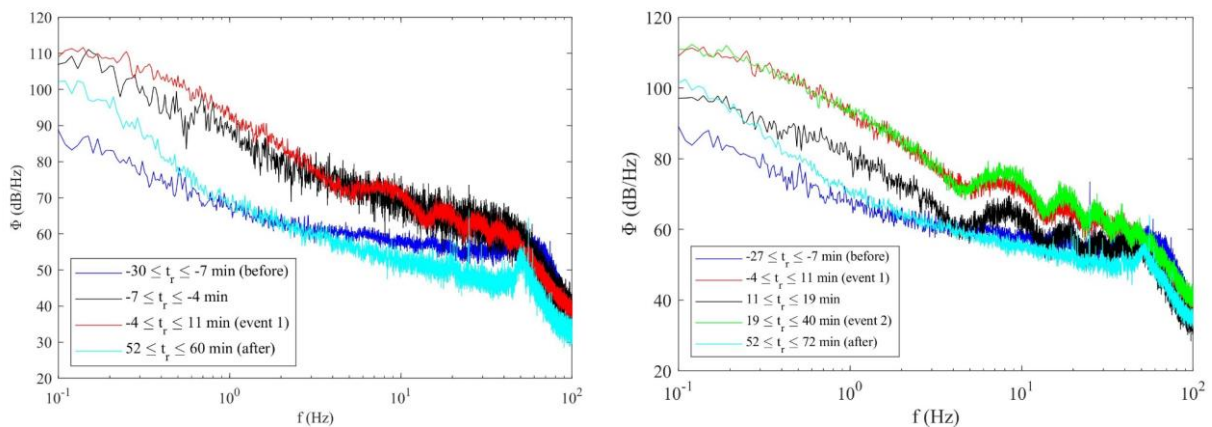

Figure 7. Comparison of the pressure power spectra (a) immediately before event 1 with event 1 and (b) during the infrasound burst events as well as the period between the events. As a reference, the mean spectrum before and after the period of interest are provided in both figures.

These spectra also show that the majority of the signal observed in the time trace (Figure 4) was due to the content below 5 Hz, which is the portion that does not produce the tones. It was previously stated that this elevated lower frequency content was likely due to wind noise, which is assessed in more detail here by comparing the integrated sound pressure over specific bands to the local wind speed. Unfortunately, the weather

station at the infrasound site (DML) was averaging over a 30-minute period, which is too long to make a meaningful comparison during this event. Consequently, the integrated sound pressure is compared against the wind speeds measured at the closest Mesonet site (STIL) in Figure 8. The maximum wind speed during the 5-minute interval was used as the wind speed with the error bars corresponding to the standard deviation of the wind speed during that period. Figure 8a shows the sound pressure integrated from 0.1-5 Hz while Figure 8b integrates over the 5-50 Hz band (i.e. the band that produced the tones of interest). This shows that the 0.1 to 5 Hz band is well correlated with wind speed with a significant rise above the background occurring when the speed exceeds ~5 m/s. This is consistent with Pepyne & Klaiber (2012) that observed that porous hose filters were not effective windscreens when the wind exceeds 5 m/s. Conversely, the 5-50 Hz band has negligible variation at speeds approaching 10 m/s. The only data points that are significantly above the background in Figure 8b are those corresponding to measurements during events 1 and 2. Also note that during event 1, the 5-50 Hz band has negligible variation in integrated sound pressure versus wind speed (trend is actually negative). This shows that the frequency content below 5 Hz is primarily due to wind noise while the 5-50 Hz was not wind noise.
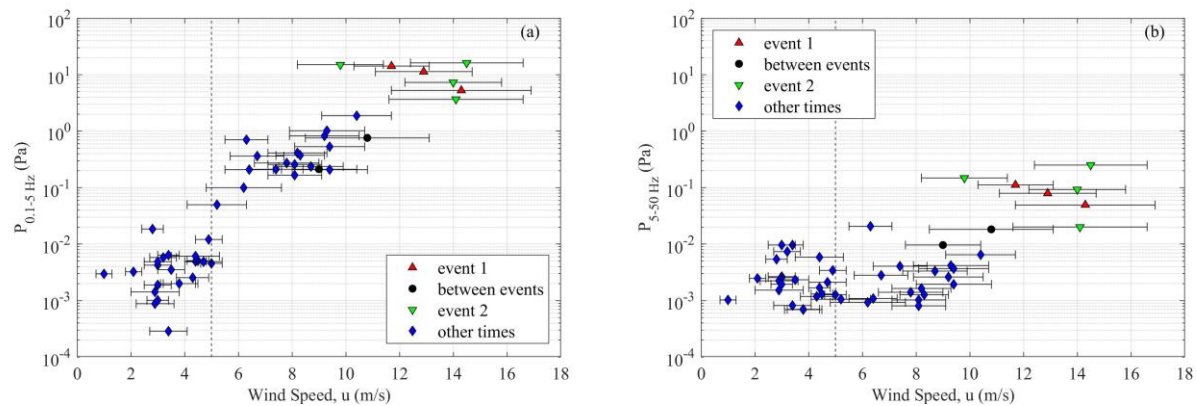

Figure 8. Integrated sound pressure from (a) 0.1-5.0 Hz and (b) 5-50 Hz plotted versus the maximum wind speed at the Stillwater Mesonet site. The error bars correspond to the standard deviation during the given 5-minute interval. The vertical dashed lines mark the 5 m/s wind speed.

III. BEARING ANGLE

Given that the larger amplitude content was associated with wind noise, the question is narrowed to whether the band that produced the tones was associated with the tornado. The cross-talk contamination between microphones 2 and 3 prevents bearing angle calculation without applying assumptions about the resulting pressure wave and its orientation. However, it is possible to answer the question of whether the received signals are consistent with what is expected if they were produced by the tornado. For this analysis it is assumed that the distance between the tornado and the array (18.7 km) was sufficient that the received signals are well approximated as plane waves. Given the speed of sound (343.8 m/s; mean from STIL, DML, PERK) and the frequency range of interest ($5 < f < 14$ Hz), the distance between the array and tornado corresponds to 270 to 760 wavelengths. Next it is assumed that the received signals were propagating parallel to the ground directly from the source. Note that given a range of 18.7 km with possible cross-wind propagation, this assumption adds uncertainty to the calculations. The bearing angle of the filtered signal was determined with time-domain beamforming using the time difference of arrival technique (Dowling & Sabra, 2015). The cross-correlation between microphones 1 and 3 was performed with the maximum time lag of interest corresponding to the distance between microphones 1 and 3 (L_{13}) divided by the speed of sound (c). The separation (or lag) time corresponding to the maximum correlation was used to determine the separation time between microphones 1 and 3 ($t_{13} = t_1 - t_3$). Given the assumptions listed above, there are two possible bearing angles associated with this separation time with each mirrored about the line between microphones 1 and 3. (Note that if the horizontal plane wave assumption were not applied this would represent a cone). This separation time was then used to determine the angle between the plane wave front and the line connecting microphones 1 and 3,

$$\theta = \cos^{-1}\left(\frac{c|t_{13}|}{L_{13}}\right).$$

The definitions of the angles of interest are illustrated in Figure 9. The angle measured from the line connecting microphones 1 and 3 to the direction of the advancing pressure wave (ϕ) as well as the mirrored result (ϕ') are

$$\left.\begin{array}{l} \phi = \theta \\ \phi' = 2\pi - \theta \end{array}\right\} \text{ for } t_{13} \leq 0$$

$$\left.\begin{array}{l} \phi = \pi - \theta \\ \phi' = \pi + \theta \end{array}\right\} \text{ for } t_{13} \geq 0.$$

These two angles combined with the fixed angle between north and the line connecting microphones 1 and 3 ($\alpha = 53.4°$) are sufficient to determine the bearing angle (φ) of the received signal measured clockwise from north ($0°$),

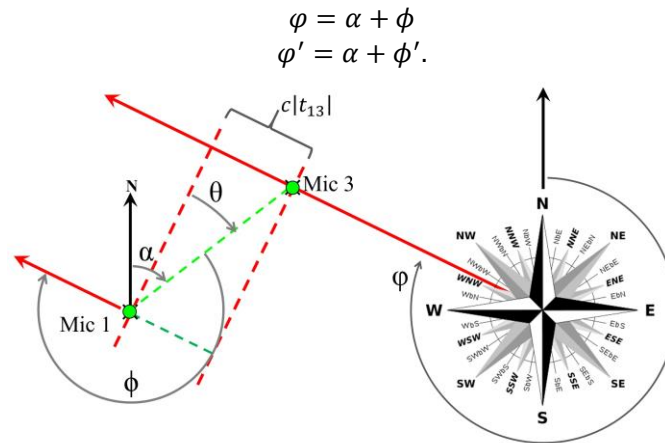$$\varphi = \alpha + \phi$$
$$\varphi' = \alpha + \phi'.$$

Figure 9. Schematic illustrating the definitions of angles used to determine the bearing angle of the received signal.
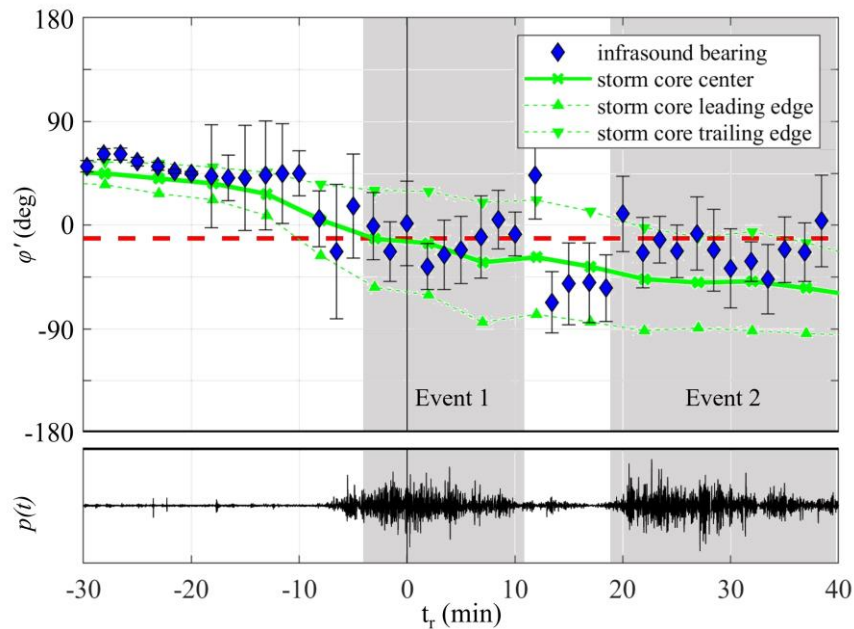

Figure 10. Bearing angle (φ') of the received signal bandpass filtered between 5-50 Hz. The horizontal red dashed line is the tornado bearing angle. The green dashed lines correspond to the nominal bearing angles of the leading or trailing edges of the storm core while the solid line is the storm core center. Sound pressure time trace is also included for reference. In addition, the periods corresponding to infrasound events 1 and 2 are shaded.

It was found that the resulting bearing angle was most sensitive to the processing parameters, which produced the largest uncertainty in the above analysis. Thus the bearing angle was computed by applying a 5th order Butterworth bandpass filter with the minimum and maximum cutoff frequencies incrementally varied between 5.5-11.5 Hz and 40-50 Hz, respectively. These frequency ranges were selected because they nominally span the width of the fundamental peak and the 4th overtone, respectively. In addition, the segment period and

overlap percentage between segments was varied, which produced a total of 189 computed bearing angles per time step. In Figure 10, the resulting time history of the mean bearing angle for the received infrasound signals is shown with the error bars equal to the standard deviation determined from variation of the processing parameters. Note that to avoid phase wrapping near the time when the tornado was present, the results are plotted with $-180° < \varphi' \leq +180°$. Also, for clarity only φ' is shown in Figure 10 since this analysis is simply to show that the directionality of the received signals are consistent with that expected from the tornado. For comparison, the relative bearing angles for the front, middle, and back side of the storm core that produced the tornado are also provided in Figure 10. Here the 'storm core' location was defined via radar reflectivity as the region of the storm that produced the tornado with > 50 dBZ at a nominal elevation of 1 km. In addition, a horizontal reference line at the bearing angle corresponding to the tornado report ($\varphi_{tornado} = -11.5°$) is included, which intersects the storm core center curve at $t_r = 0$. It should be noted that at ~2035 UTC ($t_r \approx 22$ min) the storm core breaks into two segments with the bearing angles shown corresponding to the front and back of the leading and trailing segments, respectively. While there is significant scatter in the results, the mean bearing angles clearly track with the general storm core direction with the majority of data points falling between the bearing angles corresponding to the leading and trailing edges of the storm core that produced the tornado. Ultimately, given the applied assumptions, the bearing angles are nominally consistent with what would be expected if emitted from the verified tornado location. This gives corroborative evidence that the infrasound signal of interest originated from the region within the storm that produced the tornado.

B.   COMPARISON WITH ABDULLAH (1966)

Assuming the received signal was from the tornado, this is one of the first documentations of overtones associated with a tornado. Noble & Tenney (2003) also reported spectra that appeared to have overtones, but no detailed analysis of the signal was provided. While the current work does not aim to attribute the observations to a specific mechanism, it is useful to compare to the theory proposed in Abdullah (1966) since it predicts non-integer overtones of a fundamental frequency. Abdullah (1966) modeled a tornado as a compressible Rankine vortex, which when constrained to axisymmetric vibrations with a large vertical-to-radial wavelength ratio provides a simple relationship between the nth mode frequency (f_n) and tornado size,

$$f_n = \frac{(4n + 5)c}{4d}. \tag{2}$$

Here n is a non-negative integer, c is the speed of sound, and d is the diameter of the vortex core. Before the comparison it is important to note that Schecter (2012) has demonstrated that the Abdullah (1966) analysis has fundamental issues; primarily (i) constraints on the tangential velocity fluctuations at $d/2$ are nonphysical, (ii) requirements on outward propagation of acoustic waves are not met, and (iii) the solution includes modes for nonphysical acoustic sources outside of the vortex. The current fundamental frequency can be compared against the predictions of Abdullah (1966) if a reasonable estimate of the vortex core can be obtained. The only data available for this tornado was that the maximum damage path width was 46 m and there is a low quality video of the tornado that shows the maximum width of the visible funnel cloud being ~2.9 times the width at the ground. If the maximum damage path width was set as the vortex core diameter, Abduallah (1966) predicts a fundamental frequency of 8.6 Hz, which is close to the current observation (8.3 Hz) and matches almost exactly with that predicted by (3). However, the damage path width is a poor estimate of the vortex core and in general past observations (Bedard, 2005; Dunn et al., 2016) have aligned better with the first or second harmonics predicted by Abdullah (1966).

In Figure 11, the overtones from the current observations are compared with prediction from (2) with the vortex core diameter was fixed by using the speed of sound ($c = 343.8$ m/s) and matching the fundamental frequency (8.3 Hz). The error bars on the current results are set based on the quality factor (i.e. 3-dB reduction on each side of the peak). Given the fundamental issues (Schecter, 2012), it is not surprising that (2) does not accurately predict the current results. The linear best fit curve to the current results is

$$f_n = 9.47n + 8.64. \tag{3}$$

Linear regression analysis shows that both the slope (9.47 ± 0.56) and intercept (8.64 ± 1.38) were statistically significant (p-value < 0.05). Furthermore, using a t-test on the slope shows that the multiplication factor between overtones was between 1.07 and 1.21 with 95% confidence. Thus the current results show a linear relationship between non-harmonic overtones. This is a potentially important observation with respect to identifying a fluid mechanism for the infrasound production.
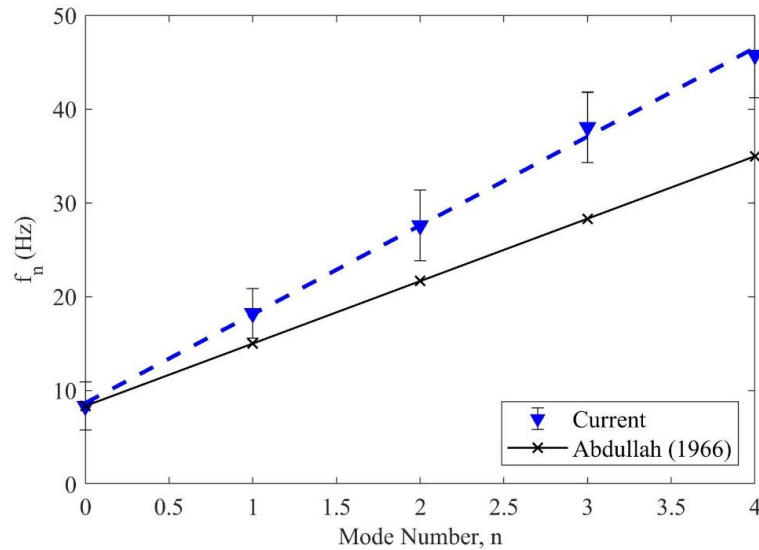
Figure 11. Fundamental and overtones during infrasound event 1 (tornado) compared with the predictions from equation (2) given the fundamental frequency.
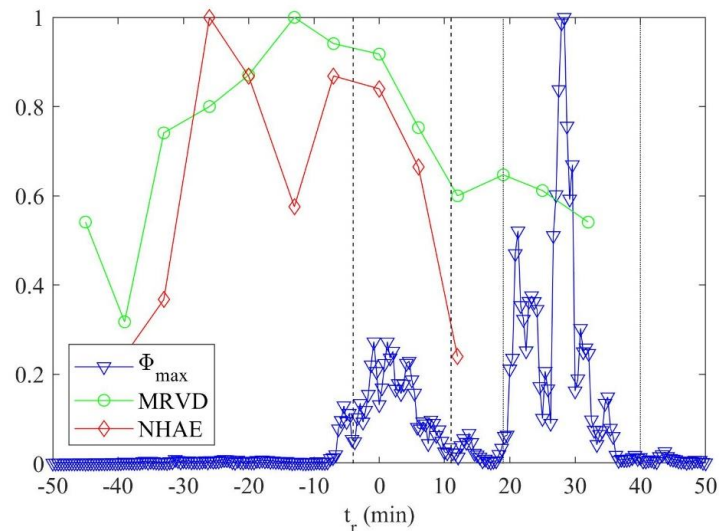
C. COMPARISON WITH RADAR METRICS

Figure 12. Time histories of the normalized pressure power spectra within the 5-14 Hz band (Φ_{max}), maximum radial velocity difference (MRVD), and the normalized hail areal extent (NHAE). Vertical dashed and solid lines denote the windows corresponding to infrasound event 1 and 2, respectively.

Finally, the radar metrics previously discussed, maximum radial velocity difference (MRVD) and normalized hail areal extent (NHAE), are compared with the peak in the power spectra within the 5-14 Hz band, Φ_{max} (i.e. fundamental frequency). These results are shown in Figure 12 with each parameter normalized to facilitate comparisons. The maximum values used to scale the maximum pressure power spectra (Φ_{max}), MRVD, and the NHAE were 0.3123 Pa^2/Hz, 42.5 m/s, and 0.137, respectively. The peak in MRVD occurs before any significant rise in infrasound, which shows that infrasound production was not well correlated with the large-scale rotation of the supercell that produced the tornado. Comparison with NHAE is interesting because there is a history of observations indicating a complex relationship between hail production, vorticity, and infrasound production (Bowman & Bedard, 1971; Bedard, 2005; Schecter et al., 2008). The power spectral peak in the 5-14 Hz band (Φ_{max}) for the current observation has a general trend with NHAE during event 1 with their rise, peak, and roll off occurring at approximately the same time. Schecter et al. (2008) results indicate that infrasound from a tornado-like vortex radiates infrasound in the 0.1-10 Hz band from the region where diabatic processes involving hail are active, which would suggest a potential connection between them. However, NHAE achieved

a maximum (evident from both the radar metric and hail reports) before the infrasound was observed. This is consistent with past observations that infrasound is often observed with hail-producing storms (Bowman & Bedard, 1971) and that hail-producing storms with no vorticity do not produce infrasound (Bedard, 2005). Ultimately these results suggest that infrasound from a tornadic storm could be connected with hail production, but hail production is not solely responsible for the infrasound production.

5. CONCLUSIONS

The current work presents infrasound measurements during a hail-producing supercell in Oklahoma on 11 May 2017, which produced an EFU tornado near Perkins, OK (35.97, -97.04) at 2013 UTC with a path length of 0.16 km and damage path width of 46 m. The infrasound was contaminated by wind noise at frequencies below 5 Hz, but the signal was above the background noise in the 5-50 Hz band. The received signals were consistent with the movement of the tornado-producing storm. The power spectra showed that a fundamental frequency of 8.3 Hz was produced with linearly related overtones (18, 29, 36, and 44 Hz). The overtones were not pure harmonics (factor of 1.1 between frequencies), which Abdullah (1966) predicts non-harmonic overtones and a fundamental frequency using the maximum damage path width (8.6 Hz) that is close to that observed (8.3 Hz). However, the observed overtones do not match the prediction of Abdullah (1966), the use of the maximum damage path width is not equivalent to vortex core, and most other observations in the literature do not align with the predicted fundamental frequency. Consequently, while the similarities are intriguing, the fundamental issues identified in Schecter (2012) combined with the observed deviations preclude Abdullah (1966) from being a potential explanation for the infrasound production. Finally, the comparison with radar metrics shows that the infrasound was not produced by the large-scale mesocyclone rotation and hail production could be connected with infrasound production though hail production alone cannot explain the observations.

ACKNOWLEDGMENTS

REFERENCES

Abdullah, A. J. (**1966**). "The musical sound emitted by a tornado," *Mon. Weather Rev.*, **94**, 213-220.

Bedard, A. J. (**2005**). "Low-frequency atmospheric acoustic energy associated with vortices produced by thunderstorms," *Mon. Weather Rev.*, **133**(1), 241-263.

Bedard, A. J. and Georges, T. M. (**2000**). "Atmospheric infrasound," *Phys. Today*, **53**(3), 32-37.

Bendat, J. S. and Piersol, A. G. (**2000**). *Random Data: Analysis and Measurement Procedures*. 3rd Edition (John Wiley & Sons, New York), 457-477.

Bowman, H. S. and Bedard, A. J. (**1971**). "Observations of infrasound and subsonic disturbances related to severe weather," *Geophys. J. Int.*, **26**, 215-242.

Brock, F. V., Crawford, K.C., Elliott, R. L., Cuperus, G. W., Stadler, S. J., Johnson, H. L. and Eilts, M. D. (**1995**). "The Oklahoma Mesonet: A technical overview," *J. Atmos. Ocean. Tech.*, **12**, 5-19.

Browning, K. A. (**1965**). "The evolution of tornadic storms," *J. Atmos. Sci.*, **22**, 664-668.

Cramer, O. (1993). "The variation of the specific heat ratio and the speed of sound in air with temperature, pressure, humidity, and CO_2 concentration," *J. Acoust. Soc. Am.*, **93**(5), 2510-2516.

Doviak, R. J. and Zrnić, D. S. (**2006**). *Doppler Radar and Weather Observations*. 2nd Edition, pp. 562 (Dover Publications, New York).

Dowling, D. R. and Sabra, K. G. (**2015**). "Acoustic remote sensing," *Annu. Rev. Fluid Mech.*, **47**, 221-243.

Dunn, R. W., Meredith, J. A., Lamb, A. B. and Kessler, E. G. (**2016**). "Detection of atmospheric infrasound with a ring laser interferometer," *J. Appl. Phys.*, **120**, 123109-7.

Elbing, B. R. and Gaeta, R. J. (**2016**). "Integration of infrasonic sensing with UAS (invited)," AIAA Aviation, AIAA2016-3581, Washington, DC (June 13-17) (doi:10.2514/6.2016-3581).

Frazier, W. G., Talmadge, C., Park, J., Waxler, R. and Assink, J. (**2014**). "Acoustic detection, tracking, and characterization of three tornadoes," *J. Acoust. Soc. Am.*, **135**(4), 1742-1751 (doi: 10.1121/1.4867365).

Hart, D. and McDonald, T. (**2009**). "Infrasound sensor and porous-hose filter evaluation results," *Proc. of the Monitoring Res. Rev.: Ground-Based Nuclear Explosion Monitoring Tech.*, Vol. II, 6-05, 735-741.

Jacob, J. D., Chilson, P. B., Houston, A. L. and Smith, S. W. (**2018**). "Considerations for atmospheric measurements with small unmanned aircraft systems," *Atmosphere*, **9**(7), 252-16.

Le Pichon, A., Blanc, E. and Hauchecorne, A. (**2010**). *Infrasound Monitoring for Atmospheric Studies*, 1st Edition (Springer, New York).

McPherson, R. A., Fiebrich, C., Crawford, K. C., Elliott, R. L., Kilby, J. R., Grimsley, D. L., Martinez, J. E., Basara, J. B., Illston, B. G., Morris, D. A., Kloesel, K. A., Stadler, S. J., Melvin, A. D., Sutherland, A. J. and Shrivastava, H. (**2007**). "Statewide monitoring of the mesoscale environment: A technical update on the Oklahoma Mesonet," *J. Atmos. Ocean. Tech.*, **24**, 301–321.

NOAA (**2017**). "NOAA NCEI Storm Event Database," OK/Payne/May 11, 2017/Tornado, National Oceanic and Atmospheric Administration (NOAA), www.ncdc.noaa.gov/stormevents. Accessed May 31, 2019.

NOAA (**2018**). "Tornado warnings (nation)." National Oceanic and Atmospheric Administration (NOAA), https://verification.nws.noaa.gov/services/gpra/NWS_GPRA_Metrics.pdf. Accessed on May 13, 2019.

Noble, J. M. and Tenney, S. M. (**2003**). "Detection of naturally occurring events from small aperture infrasound arrays," in *Battlespace Atm. & Cloud Impacts on Military Operations Conf.*, Monterey, CA (Sept 9-11).

Pepyne, D. L. and Klaiber, S. (**2012**). "Highlights from the 2011 CASA infrasound field experiment," in *The 92nd American Meteorological Soc. Annual Meeting*, IOAS-AOLS 2.4, New Orleans, LA (Jan 22-26).

Schecter, D. A. (**2012**). "A brief critique of a theory used to interpret the infrasound of tornadic thunderstorms," *Mon. Weather Rev.*, **140**(7), 2080-2089.

Schecter, D. A., Nicholls, M. E., Persing, J., Bedard Jr., A. J. and Pielke Sr., R. A. (**2008**). "Infrasound emitted by tornado-like vortices: Basic theory and a numerical comparison to the acoustic radiation of a single-cell thunderstorm," *J. Atmos. Sci.*, **65**, 685-713.

Shams, Q. A., Zuckerwar, A. J., Burkett, C. G., Weistroffer, G. R. and Hugo, D. R. (**2013**). "Experimental investigation into infrasonic emissions from atmospheric turbulence," *J. Acoust. Soc. Am.*, **133**(3), 1269-1280 (doi: 10.1121/1.4776180).

Smith, S. W., Chilson, P. B., Houston, A. L. and Jacob, J. D. (**2017**). "Catalyzing collaboration for multi-disciplinary UAS development with a flight campaign focused on meteorology and atmospheric physics," in *AIAA Information Systems-AIAA Infotech @ Aerospace*, AIAA-2017-1156.

Threatt, A. (**2016**). "Investigation of natural and anthropomorphic sources of atmospheric infrasound," M.S. Thesis, Oklahoma State University, Stillwater, OK.

Van Den Broeke, M. S. (**2017**). "Polarimetric radar metrics related to tornado life cycles and intensity in supercell storms," *Mon. Weather Rev.*, **145**, 3671-3686.

Van Den Broeke, M. S., Straka, J. M. and Rasmussen, E. N. (**2008**). "Polarimetric radar observations at low levels during tornado life cycles in a small sample of classic Southern Plains supercells," *J. Appl. Meteorol. Clim.*, **47**, 1232-1247.

Waxler, R. M. and Assink, J. D. (**2017**). "NCPAprop – A software package for infrasound propagation modeling," *J. Acoust. Soc. Am.*, **141**, 3627.